scientific reports

Check for updates

OPEN

Simulation and analysis of the CO_2 range-resolved differential absorption lidar system at 2 μm

Bowen Zhang[1,2], Guangqiang Fan[1]✉ & Tianshu Zhang[1]✉

The range-resolved differential absorption lidar is a high-precision device to measure the concentration of carbon dioxide. This paper provides a system-wide theoretical analysis method for the performance analysis and parameter optimization of the lidar system using the given parameter range. The scattered echo signal, signal-to-noise ratio, and detection sensitivity were simulated by setting assumed parameters with the HITRAN 2020 database and the US 1976 standard atmosphere model to analyze the detection distance and concentration resolution of the lidar system. The effects of the laser energy, repetition frequency, and photodetector noise were also discussed. The wavelength selection near the absorption line is critical because it controls the height region of the highest sensitivity and the demands on frequency stability. Recommendations for the selection of absorption lines are provided in this paper. A quantitative analysis of each error source provided reasonable error ranges.

Carbon dioxide (CO_2) is considered a significant contributor to greenhouse gases. It results from various human production and living processes. Due to diverse interactions with various climate components, such as the atmosphere, biosphere, and hydrosphere, CO_2 has a notable involvement in the Earth's climate. These interactions identify CO_2 sources and sinks that affect the global gas transport fluxes[1–3].

To detect CO_2, there are two differential absorption lidar (DIAL) techniques: integrated-path DIAL (IPDIAL) and range-resolved DIAL (RRDIAL). Several spaceborne IPDIAL systems for CO_2 detection were developed by NASA and ESA with 1.57- and 2.05-μm wavelengths[4–9]. The carbon dioxide satellites like the OCO-2/3 and GOSAT required sunlight exposure and cloudless conditions. Their observations in the tropical terrestrial biosphere, high latitude regions of the Northern Hemisphere, and the Southern Ocean were still limited and had significant deviations[10,11]. China's first carbon dioxide measurement satellite mission, TanSat, has a hyperspectral grating spectrometer that covers the near-infrared and shortwave infrared regions sensitive to carbon dioxide absorption. The minimum footprint size measured by TanSat is approximately 2×2 km^2, with 9 footprints crossing the track within a framework. This means that TanSat has the potential to capture anthropogenic emission enhancements downstream of cities and power plants[12]. Campbell evaluated the concentration of carbon dioxide using an airborne IPDIAL based on 1.57 μm and found that the bias of the atmospheric column CO_2 concentration within 1 h of flight time was less than 1ppm[13]. Yu used a 1.57-μm coherent DIAL to measure 3-D CO_2 and wind fields simultaneously. In a range resolution of 120 m and time resolution of 60 s, the longest detection range of CO_2 is 6 km. The accuracy of CO_2 detection is a mean and standard deviation of 2.05 ppm and 1.78 ppm[14]. Korch provided a laser at a 2.05-μm wavelength with a coherent heterodyne receiver. The coherent detection performance was analyzed, and the concentration precision was 1–2% over the column lengths[15]. Gibert showed a coherent DIAL (CDIAL) system to detect CO_2 at 2 μm with high time and space resolution and the additional capability for wind profiling. The CDIAL provided a 150-m range and a 15-min time-resolved CO_2 absorption coefficient with an instrumental error of 0.5% at 500 m[16].

According to its principle, IPDIAL can only obtain the column concentration of CO_2, and cannot be applied to measure the carbon flux for surface sources or detect unorganized emission sources. However, this measurement can be achieved by using a high-precision RRDIAL. Currently, the 1.5-μm wavelength is primarily used by many researchers for IPDIAL detection. The mid-infrared band at 2 μm provides the potential for increasing the transmitted laser energy while maintaining eye-safety requirements, which enables a longer operating range with higher sensitivities. As technology has advanced in recent years, single-frequency lasers, infrared detectors, and other optical and electronic pieces of equipment have become increasingly mature and reliable. CO_2 has a

[1]Anhui Institute of Optics and Fine Mechanics, Hefei Institutes of Physical Science, Chinese Academy of Sciences, Hefei 230031, China. [2]University of Science and Technology of China, Hefei 230026, China. ✉email: gqfan@aiofm.ac.cn; tszhang@aiofm.ac.cn

larger absorption effect at 2 μm than 1.5 μm, which makes it more suitable for achieving high precision of the RRDIAL detection. Although some papers on the lidar system design have been published at 2 μm, they only analyze some of the error sources and lack the overall analysis process for the direct detection RRDIAL system; meanwhile, several existing papers are based on the 1.5-μm IPDIAL technique and partial error analysis[17,18]. Applying coherent detection overcomes the lack of photodiode sensitivity at this wavelength. However, the drawback of coherent heterodyne detection includes the speckle noise that limits the precision of the DIAL system, increased complexity, and increased cost.

This paper provides a comprehensive systematic analysis solution by discussing the selection of wavelength, simulating the system detection capability, evaluating the performance, and analyzing the influence and sources of random and systematic errors in the direct detection system.

DIAL principle and method

Theoretical principle of DIAL

The direct detection RRDIAL system sequentially emits two pulsed waves. The off-line wavelength is far from the center of the absorption line and only weakly attenuated by the absorption, whereas the on-line wavelength is near the center of the absorption line and mainly attenuated because it is absorbed by the CO_2 during propagation through the atmosphere[19]. Measurements are based on the Rayleigh and Mie backscattering from the atmospheric molecular and aerosol, and the analysis of the difference in on and off signal provides range-resolved measurements of the CO_2 concentration. The schematic illustration of the DIAL system is shown in Fig. 1.

The on-line and off-line wavelengths are carefully selected to avoid interference from other molecules except for CO_2. These wavelengths are so similar to one another that the effects of scattering and absorption by aerosols and atmospheric molecules are negligible, which implies that different intensities of the echo signal are mainly caused by CO_2 absorption in the atmosphere. The echo power is given by the simplified lidar equation according to the remote sensing principle[20–23], which can be written as:

$$P_r(R) = P_0 \frac{c\tau}{2} A\eta \frac{\beta(R)}{R^2} \xi(R) \exp\left\{-2\int_R^{R+\Delta R} [N_{CO2}(r)\sigma(r) + \alpha(r)]dr\right\}, \tag{1}$$

where P_r is the echo power of λ_{on} or λ_{off}, P_0 is the transmitted power of the single-frequency laser, c is the speed of light, τ is the laser pulse width, A is the telescope area of primary receiver optics responsible for the collection of backscattered light, η is the total optical efficiency and represents the total transmittance of the various optics used in the system, R is the detection range, ΔR is the range resolution, β is the backscatter coefficient and denotes the ability of the atmosphere to scatter light back into the direction from which it comes, ξ is the overlap function that can take values of 0–1, N_{CO2} is the number density of CO_2 at distance R, σ is the absorption cross-section of the CO_2, and α is the atmospheric extinction coefficient, which describes how much light is lost on the way from the lidar to distance R and back. Factor *2* denotes the two-way transmission path in the integral.

The lidar equation demonstrates that the echo signal intensity is inversely proportional to the squared distance. This relationship results in significant differences in the intensity of the short-distance and long-distance echo signals. The dynamic range of the lidar signal is substantial. To compress the near-field signal, we can adjust the overlap function. Several orders of magnitude can be used to suppress the strong near-field signal, which can reduce the requirements for the detector.

The atmospheric extinction coefficient and backscatter coefficient are roughly equal at selected wavelengths when the on-line and off-line wavelengths are relatively close together. The lidar function is subjected to differential and logarithmic operations, and the number density of CO_2 can be expressed by:

$$N_{CO2} = \frac{-1}{2\Delta\sigma} \frac{d}{dr} ln \frac{P_r(\lambda_{on}, r+\Delta r) P_r(\lambda_{off}, r)}{P_r(\lambda_{on}, r) P_r(\lambda_{off}, r+\Delta r)}, \tag{2}$$

where $\Delta\sigma$ is the differential absorption cross-section between on-line and off-line wavelengths. The differential optical depth (DAOD) is:

$$\Delta\tau = \tau_{on} - \tau_{off} = \int_R^{R+\Delta R} N_{CO2}(r)\Delta\sigma(r)dr = -\frac{1}{2} ln \frac{P_r(\lambda_{on}, r+\Delta r) P_r(\lambda_{off}, r)}{P_r(\lambda_{on}, r) P_r(\lambda_{off}, r+\Delta r)}, \tag{3}$$

The optical depth (OD) is a dimensionless quantity that characterizes the degree of absorption of laser energy by CO_2.

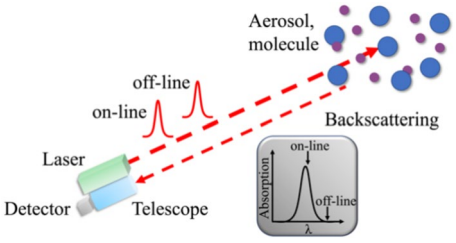

Figure 1. Schematic illustration of the DIAL system.

Methods to evaluate the system performance

The performance of RRDIAL is affected by aerosol, atmospheric molecules, background radiation, and instrument noises. When the signal-to-noise ratio (SNR) is low, due to the strong noise or the weak signal, the analysis results can have serious distortion. Generally, the echo signal photocurrent is obtained by deducting the photodetector dark current and background radiation photocurrent from the anode current[23,24]:

$$i_s = (i_s + i_b + i_d) - (i_b + i_d), \tag{4}$$

where i_s is the echo signal photocurrent, i_b is the background radiation photocurrent, and i_d is the photodetector dark current. When the noises are independent of one another, the SNR of the output by the photodetector can be expressed as:

$$SNR = \frac{i_s}{\Delta i_s} = \frac{i_s}{\sqrt{\overline{\Delta i_s^2} + 2\left(\overline{\Delta i_b^2} + \overline{\Delta i_d^2}\right)}}, \tag{5}$$

where $\overline{\Delta i_s^2}$, $\overline{\Delta i_b^2}$, and $\overline{\Delta i_d^2}$ are the root-mean-square values of the current in proportion as the statistical fluctuation of the echo signal, background radiation, and photodetector dark current, respectively.

According to statistical physics, the power spectral density of shot noise is related to the current i, and the root-mean-square values of the currents of shot noise generated by the optical signal, background radiation, and photodetector dark current are:

$$\begin{cases} \overline{\Delta i_s^2} = 2ei_s\Delta f \\ \overline{\Delta i_b^2} = 2ei_b\Delta f \\ \overline{\Delta i_d^2} = 2ei_d\Delta f \end{cases}, \tag{6}$$

where i_b is the average background radiation current output by the photodetector, i_d is the dark current of the photodetector, and Δf is the electronic frequency bandwidth of the photomultiplier tube. The quantum efficiency of the photodetector is:

$$\eta_q = \frac{R_v hc}{\lambda e}, \tag{7}$$

where R_v is the response rate of the photodetector, and h is the Planck constant. The noise equivalent power of the signal is:

$$NEP_s = \frac{i_s}{R_v} = \sqrt{k\frac{hc\Delta f}{\lambda\eta_q}P_r}, \tag{8}$$

The noise equivalent power of background radiation is:

$$NEP_b = \sqrt{k\frac{hc\Delta f}{\lambda\eta_q}P_b}, \tag{9}$$

P_b is the power of background noise which is $P_b = E_b\eta\Omega A\Delta\lambda$, where E_b is the background radiance, Ω is the stereo angle of the receiving field, and $\Delta\lambda$ is the filter bandwidth.

The noise equivalent power of the photodetector dark current is:

$$NEP_d = \frac{\sqrt{A_d\Delta f}}{D^*}, \tag{10}$$

D^* is the specific detectivity, A_d is the active photodetector area, and k is the scale factor (= 2 for a photovoltaic detector).

The SNR of the mid-infrared detection system can be expressed as:

$$SNR = \frac{P_r}{\sqrt{NEP_s^2 + 2\left(NEP_b^2 + NEP_d^2\right)}}, \tag{11}$$

The detection sensitivity of the system is the key indicator, which determines the minimum concentration that can be detected by the RRDIAL system at a certain range. According to the error transfer theory, if Δr is sufficiently short, it can be written as:

$$\frac{\sigma(N_r)}{N_r} = \frac{1}{\sqrt{2}\Delta\sigma\,\Delta r N_r}\sqrt{\frac{1}{SNR(\lambda_{on},r)^2} + \frac{1}{SNR\left(\lambda_{off},r\right)^2}}, \tag{12}$$

Methods of error analysis

For the direct detection RRDIAL system, the errors mainly come from the effects of the atmosphere and the laser. In essence, the absorption cross-section is changed by these factors. Since the temperature, pressure, and humidity affect the absorption of the on-line and off-line signals by CO_2, the measurement errors in their profiles will cause calculation errors.

Theoretically, the width of the gas absorption spectrum should be zero, but the absorption spectrum of substances is in fact not monochromatic due to natural broadening, pressure broadening (collision broadening), and Doppler broadening.

The energy loss in the emission radiation causes natural broadening. The change in atmospheric pressure causes pressure broadening. The sporadic movement of air molecules causes Doppler broadening. The amount of Doppler frequency shift increases with the average velocities of molecules. The spectral line broadening depends on the temperature and pressure. The pressure broadening and Doppler broadening effects should be considered in tandem because both are constantly present in the actual atmosphere. The hybrid lineaments, which are referred to as the Voigt line shape, can be expressed after the convolution of the two lineaments.

According to the US 1976 standard atmosphere model, the temperature and pressure at different heights can be obtained. This relative random error can be maintained at a minimum level if temperature-insensitive and pressure-insensitive absorption lines were selected. The absorption cross-section lines from the HITRAN 2020 database[25] at different heights were drawn as shown in Fig. 2. At various heights, the absorption cross-section gently varies; they sometimes increased and sometimes decreased. However, the relative positions of the peaks and valleys did not change. In general, there is a trend of more drastic changes with higher altitudes.

When x is the coefficient of DAOD and temperature offset and dT is the temperature offset, the relative random error (RRE) can be approximated as[26]:

$$RRE_T = \frac{\delta X_{CO2}}{X_{CO2}} = \frac{\delta \Delta\tau}{\Delta\tau} = \frac{x}{\Delta\tau} dT, \tag{13}$$

Similarly, the RRE_P caused by pressure is:

$$RRE_P = \frac{\delta X_{CO2}}{X_{CO2}} = \frac{\delta \Delta\tau}{\Delta\tau} = \frac{y}{\Delta\tau} dP, \tag{14}$$

where y is the coefficient of DAOD and pressure offset, and dP is the pressure offset.

Since the light actually emitted by the laser is not strictly monochromatic, there are lights of other frequencies near the center frequency, and the lights of these frequencies will also be absorbed by the atmospheric molecules, which will change the intensity of the echo signal and affect the inversion accuracy. Considering the central frequency of the laser and the light absorbed by the surrounding atmosphere, the effective absorption cross-section is used to replace the absorption cross-section of the ideal monochromatic laser[27,28]:

$$\sigma_{eff}(v, r) = \frac{\int L(v-v_0,r) \bullet \sigma(v,r) dv}{\int L(v-v_0,r) dv}, \tag{15}$$

where $L(v\text{-}v_0,r)$ is the spectral energy distribution of the radiation source with its center frequency v_0 which is modeled with Lorentz line shape[29]:

$$L(v) = \frac{\pi^2}{b} \frac{1}{2\cosh(2\pi^2 \frac{v}{b}) + 2\cos(\pi \frac{a}{b})}, \tag{16}$$

with the parameters $a = 1/4(1/\tau_r - 1/\tau_f)$ and $b = 1/4(1/\tau_r + 1/\tau_f)$; τ_r and τ_f are the rise time and fall time of the temporal distribution of the laser pulse, respectively. The full width at half maximum of $L(v)$ is given by $\gamma = b/\pi^2 ln((R + \sqrt{R^2 - 4})/2)$ with $R = 2(2 + cos(\pi a/b))$.

The effective absorption cross-section is affected by the linear change of laser energy, which will change the DAOD; the relative system error (RSE) can be expressed as:

$$RSE_L = \frac{\delta \Delta\tau}{\Delta\tau} = \frac{\sigma_{eff} - \sigma_{on}}{\Delta\sigma}, \tag{17}$$

The change in laser center frequency will seriously change the gas absorption intensity, and the detection results are further affected. The on-line wavelength selected by the DIAL system is on the slope near the absorption peak center, while the off-line wavelength is selected at the relatively flat absorption valley with small fluctuations. Therefore, the stability of the laser frequency is very important for high-precision measurements of the

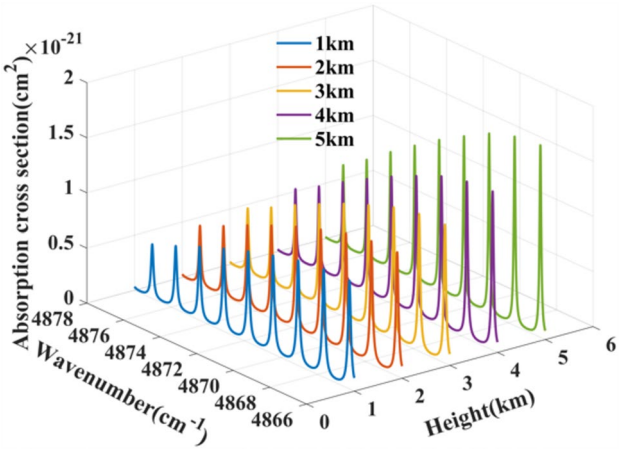

Figure 2. Absorption cross-section lines at different heights.

gas concentration. The slope method is used to estimate the measurement error caused by the frequency change, and the RSE_F caused by the laser frequency instability can be expressed as the spectral slope[30]:

$$RSE_F = \frac{1}{OD}\frac{\partial OD}{\partial F}dF, \tag{18}$$

where dF is the frequency drift.

There is a high requirement of DIAL for the quality of the laser pulse, and the pulse spectral purity is an important parameter of the laser. The spectral purity is defined as the ratio of the output energy of the laser pulse in a specific spectral range to the total energy of the pulse radiation[27]. A gas absorption cell can be used to measure the spectral purity of the laser pulse. When a monochromatic light with an initial intensity of I_0 and a frequency of v passes through an absorption cell filled with a certain uniform gas, its intensity will decay due to the gas absorption. Their relationship between them satisfies the Lambert–Beer law:

$$I(v) = I_0 \exp\left[-\int \alpha(v)dr\right], \tag{19}$$

where $\alpha(v)$ is the absorption coefficient of the detected gas. For linear absorption, $\alpha(v)$ is independent of the light intensity, and r is the absorption path length.

The spectral purity is defined as P_e, I_{seeded} is the light intensity of the seed injection mode, and I_{total} is the total light intensity of the output pulse. The calculation formula is:

$$P_e = \frac{I_{seeded}}{I_{total}} = 1 - \frac{I_{total} - I_{seeded}}{I_{total}} \approx 1 - T_{cell}, \tag{20}$$

T_{cell} is the transmittance of the long-range gas absorption cell. The energy distribution of spectral impurity is P_b, and the energy distribution of laser can be written as:

$$\widetilde{L}(v) = P_e L(v) + (1 - P_e)L_b(v), \tag{21}$$

The on-line pulse energy will be absorbed and attenuated by the target gas, but the energy of the impure part of the on-line spectrum will hardly be absorbed. Thus, the on-line echo energy will be higher than the theoretical value, and the off-line echo energy will not greatly change due to small absorption:

$$P_{on} = P_{off}\left[P_e e^{-2\Delta\tau} + (1 - P_e)\right], \tag{22}$$

The concentration inversion result caused by the spectral purity is:

$$N_{sp}(r) = \frac{-1}{2\Delta\sigma}\frac{d}{dr}\ln\left[P_e \exp(-2\Delta\tau) + 1 + P_e\right] = \frac{P_e \exp(-2\Delta\tau)}{1 - P_e + P_e \exp(-2\Delta\tau)}N(r), \tag{23}$$

And the RSE_S caused by the spectral purity is:

$$RSE_S = \frac{1 - P_e}{1 - P_e + P_e \exp(-2\Delta\tau)}, \tag{24}$$

As described above, the atmospheric parameters (temperature, pressure, water vapor, and other gases) and laser parameters (linewidth, frequency stability, and spectral purity) were considered to obtain relative errors. The total error was calculated as follows[31]:

$$\frac{\delta X_{CO2}}{X_{CO2}} = \sqrt{RRE^2 + RSE^2} = \sqrt{\left(\frac{\delta\Delta\tau_1}{\Delta\tau_1}\right)^2 + \left(\frac{\delta\Delta\tau_2}{\Delta\tau_2}\right)^2 + \cdots}, \tag{25}$$

where the subscript represents different errors.

Simulation and discussion

Selection of the CO_2 absorption line

The absorption cross-section of CO_2 in the atmosphere is affected by the wavelength stability, laser linewidth, temperature, pressure, and other substances. The system error is significantly influenced by the choice of the system wavelength. A wise choice of online and offline may lessen the influence of other factors. A smaller optical depth gives results that are only slightly different for on-line and off-line echo signals, whereas a larger optical depth produces a small on-line echo signal that is challenging to measure.

The following suggestions can be used to select the ideal pair of wavelengths[32]:

(1) Because the detected gas is the primary cause of the absorption, on-line and off-line wavelength pairs must be chosen to be sufficiently close so that the extinction of other gases can be disregarded.
(2) To reduce the density profile inaccuracy caused by temperature variations along the optical path, the chosen absorption line must only be minimally temperature dependent, especially when it is not possible to measure the temperature distribution.
(3) The on-line wavelength must have a greater absorption than the interfering gases.
(4) The control circuit can only recognize the frequency offset difference and cannot determine the direction of the frequency drift. Thus, the on-line wavelength should not be chosen at the absorption center-line, since the frequency shift is very unstable.
(5) The wavelength pairs must satisfy $|\lambda_{on}\text{-}\lambda_{off}| \leq 0.001 \times \lambda_{on}/4$.

Water vapor primarily interferes with the CO_2 absorption effect in the 2-μm range. The line-by-line radiative transfer model uses the absorption cross-section curves of CO_2 and H_2O calculated by HAPI[33] with the SDV (Speed-dependent Voigt) profile, which were retrieved from the HITRAN 2020 database and are displayed in Fig. 3a. In the calculation, the SDV profile including first-order line-mixing effects[34] was considered. Parameters such as 'LineMixing' and 'SDVoigt' were set in the *fectch_by_ids* function provided by HAPI to obtain a gas dataset. Then, the *absorptionCoefficent_SDVoigt* function was used to calculate the absorption coefficient and invert the gas absorption cross-section. As Fig. 3b shows, the absorption cross-section of CO_2 (near R30) is two orders of magnitude higher than that of H_2O, and one order of magnitude higher than the CO_2 absorption cross-section in the 1.5-μm range, which can reduce the requirement for SNR and facilitate system integration.

The wavelength pairs selected by other researchers at 2 μm are shown in Table 1. The wavelength difference between on-line and off-line is less than 1 nm. The selection of these wavelength pairs basically satisfies the five aforementioned requirements. The side-line tunable technology of the laser transmitter offers more possibilities for system design so that the lidar system can better handle various complex environments. In order to better analyze the impact of various errors, a set of wavelength pairs was randomly selected for error analysis.

Figure 3a shows that some wavelengths have a large absorption for H_2O for their location, which is not conducive to the development of a high-precision system. Figure 3b locally enlarges the location where the absorption cross-section of water vapor has a smaller and softer effect in the region, while the absorption cross-section of carbon dioxide has a relatively high effect. Considering the performance of the designed laser, the on-line position of the RRDIAL near the strong absorption region (R30 line; center-line 2050.967 nm) was selected after considering the aforementioned suggestions for the selection of absorption lines. The on-line position in this simulation analysis example was selected to be 2050.981 nm, and the off-line position was 2051.250 nm because the differential absorption of H_2O was negligible. The gentler absorption valley enables the frequency stability error of the off-line to be negligible during the simulation.

Simulation of the detection ability

The lidar equation shows that the output energy is the key factor, and its strength directly impacts the capacity of this system. The echo signal and detection distance clearly increase with a higher emitted energy. However, too much-emitted energy will damage the objects in the optical path, and the laser lifetime can be reduced. A commercial telescope with a 200-mm aperture is sufficient, and an oversized aperture will receive more background noise. The receiving field of view of the telescope should also match the divergence angle of the laser. To simulate the performance of this system, some parameters are assumed as shown in Table 2.

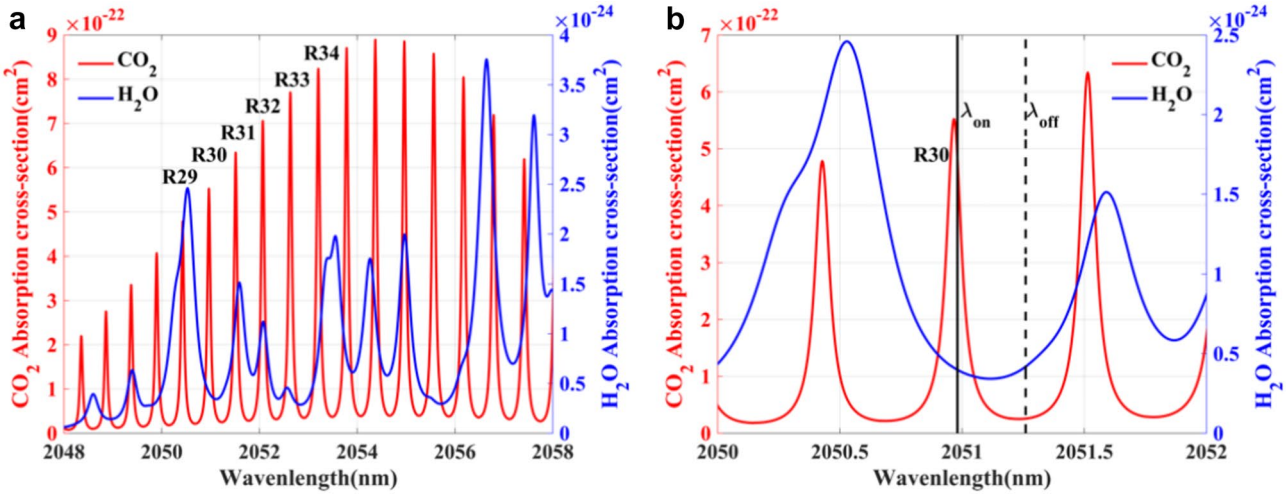

Figure 3. (**a**) CO_2 and H_2O absorption cross-section curves with wavelength obtained from the HITRAN 2020 molecular spectroscopic database; (**b**) Enlarged view of the absorption cross-section curve near R30, the solid black line represents the on-line position, and the dotted black line represents the off-line position.

Researchers	On-line (nm)	Off-line (nm)
Grady, 2008[35]	2053.228/2053.235/2053.242	2053.403–2053.410
Fabien, 2015[16]	2050.967	2051.260
Refaat, 2016[9]	2050.981/2050.995/2051.009/2051.023/2051.037/2051.051	2051.250
Erwan, 2017[36]	2050.9718	2050.8884

Table 1. Selected wavelength pairs by researchers.

Category	Parameter	Value	Unit
Transmitter subsystem	On-line wavelength	2050.981	nm
	Off-line wavelength	2051.250	nm
	Pulse energy	≥1	mJ
	Beam divergence	0.6	mrad
Receiver subsystem	Telescope diameter	200	mm
	Field of view	1	mrad
	Total optical efficiency	0.3	–
Acquisition subsystem	Quantum efficiency	0.7	–
	NEP	$\geq 1.1 \times 10^{-10}$	W
Configuration subsystem	Background radiation	2.08365×10^{-4}(on-line), 2.08125×10^{-4}(off-line)	W/(m²·Sr·nm)
	Filter bandwidth	2	nm
	Range resolution	≤120	m
	Coefficient (α, β)	From US model	-
	Absorption cross-section	From HITRAN database	-

Table 2. Assumed parameters of the RRDIAL system.

The simulated echo signal curve on the day with white noise and an overlap function can be drawn using the assumed system values[37,38]. The differential absorption cross-section of CO_2 was calculated at fixed height intervals, as it was necessary to consider that the absorption cross-section varied at different heights, which would make the simulation results closer to the real values. Figure 4a clearly shows that the long-distance echo signal intensity is 6 orders of magnitude lower than the short-distance one. The commercial photodetector should have a wide dynamic range that exceeds these values. The overlap factor in Fig. 4b shows the influence of the blind zone, transition zone, and full zone on the detection signal of the lidar in the detection process.

The SNR and sensitivity curves can be obtained as shown in Fig. 5. The minimal altitude at 4 km of the on-line signal, where the effective signal can be picked up while SNR > 1, is the lower limit of the detection capability of the system. The improved laser energy, geometric factor, total optical efficiency, and photodetector noise are required to achieve a greater SNR. Based on different pulse PRF values, a larger PRF helps realize a longer detection distance. The accumulation time can be reduced by increasing the system repetition frequency to achieve high-time resolution. According to the datasheet provided by mainstream manufacturers such as *Vigo Photonics* and *Infrared Associates*, a smaller *NEP* corresponds to better performance of the commercial photodetector. Reducing the field of view can also increase the SNR, but the receiving field angle must coincide with the laser divergence angle. The receiver field-of-view is slightly larger than the emitter divergence angle. The distribution of the sensitivity curve indicates that there is high-precision measurement accuracy at a lower height. The detection sensitivity can be better than 0.25% at approximately 2 km. If the CO_2 concentration is 400 ppm, the detection accuracy is up to 1 ppm. This concentration resolution is quite engaged for high-range resolution. Compared with the measured data of NASA[39], the simulation system can detect a similar height, so the simulation results are reliable. The simulation detected a further height because there is an ideal process.

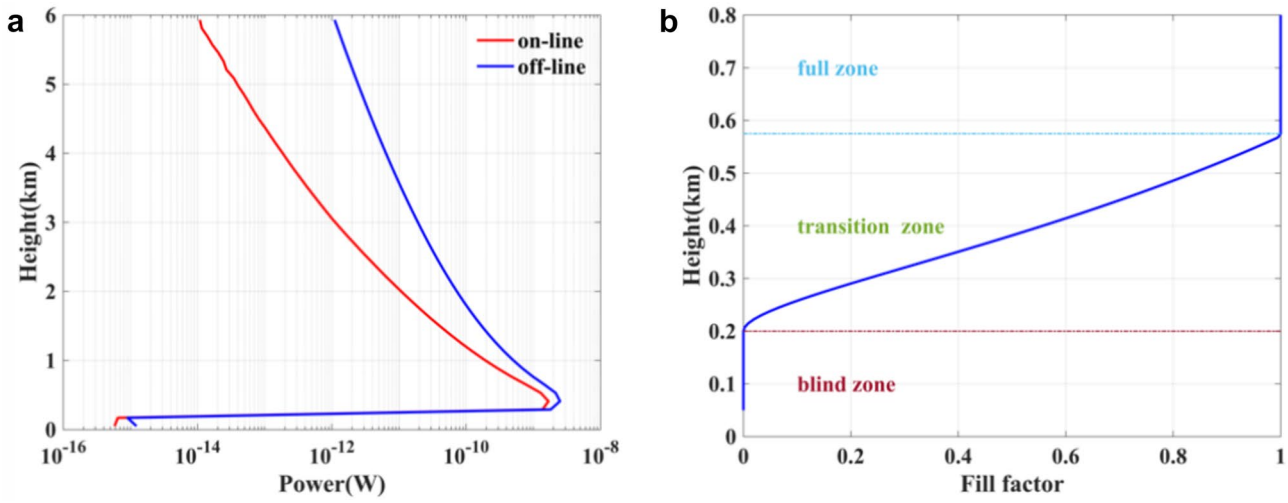

Figure 4. (**a**) Simulation of echo signal; (**b**) Overlap function.

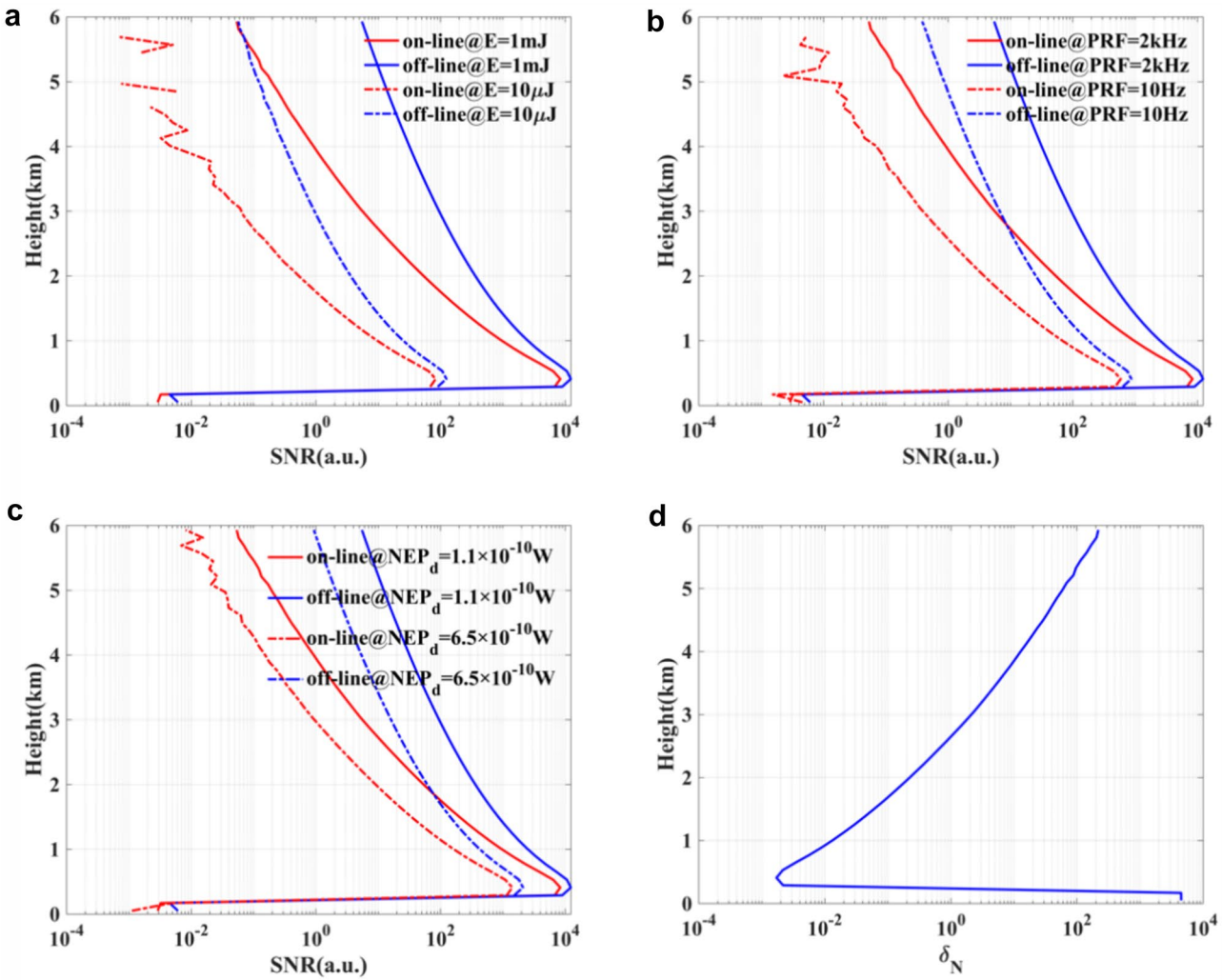

Figure 5. (**a**) Simulation of the SNR with different energies, (**b**) pulse-repetition frequencies (PRF), and (**c**) detectivities; (**d**) Detection sensitivity of the lidar system.

Relative random error

Temperature offset

Figure 6 shows RRE_T values calculated according to different temperature offsets. Figure 6a shows that the cross-section at the absorption peak will become increase while the cross-section at the absorption valley will decrease when the temperature increases. With 298 K as the standard temperature, the relative error within the temperature difference range of 0.8 K was calculated and is shown in Fig. 6b. Under identical temperature deviations, the RRE_T values caused by the positive and negative temperature deviations are basically identical. When the lidar system detects a signal in the practical atmosphere, the RRE_T caused by the temperature is less than 0.25% if the range of ambient temperature change range is less than ± 0.7 K in a short time.

Pressure offset

The RRE_P can be calculated and drawn as shown in Fig. 7. Contrary to the influence of temperature, the cross-section at the absorption peak will decrease and the absorption valley will increase when the pressure increases as shown in Fig. 7a. Figure 7b shows that the pressure offset is roughly linear with RRE_P when the pressure offset increases and the concentration inversion error will also increase. If the pressure offset is less than ± 0.003 atm when the atmospheric environment is more stable, the inversion error is less than 0.25%. Therefore, it is necessary to choose a pressure-insensitive detection wavelength pair.

Interference of other gases

H_2O, CH_4, and N_2O significantly impact the ability to detect CO_2. The individual absorption cross-section curves of these gases are shown in Fig. 8. Although the water vapor absorption has a small cross-section, the amount of water vapor in the atmosphere is relatively high, which significantly impacts the measurement results. The differential absorption cross-section of H_2O between on-line and off-line is 1.32×10^{-26} cm^2; when the air humidity is less than 100%, the water vapor concentration is approximately 27,616 ppm, which is approximately 69 times

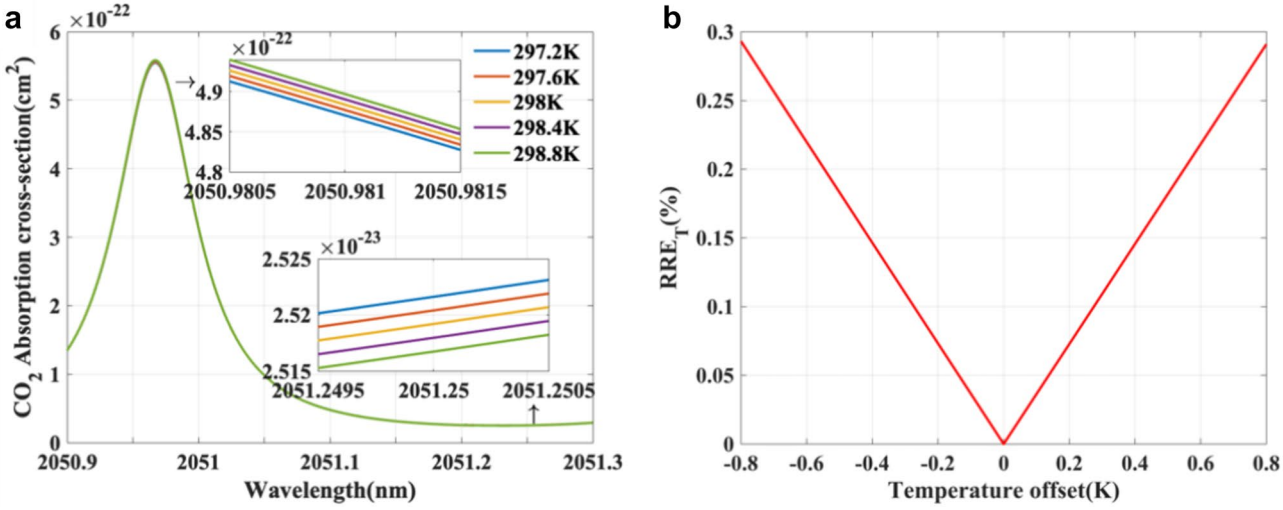

Figure 6. (**a**) Local magnification at the absorption peak and absorption valley with different temperatures; (**b**) Relationship between RRE_T and temperature offset.

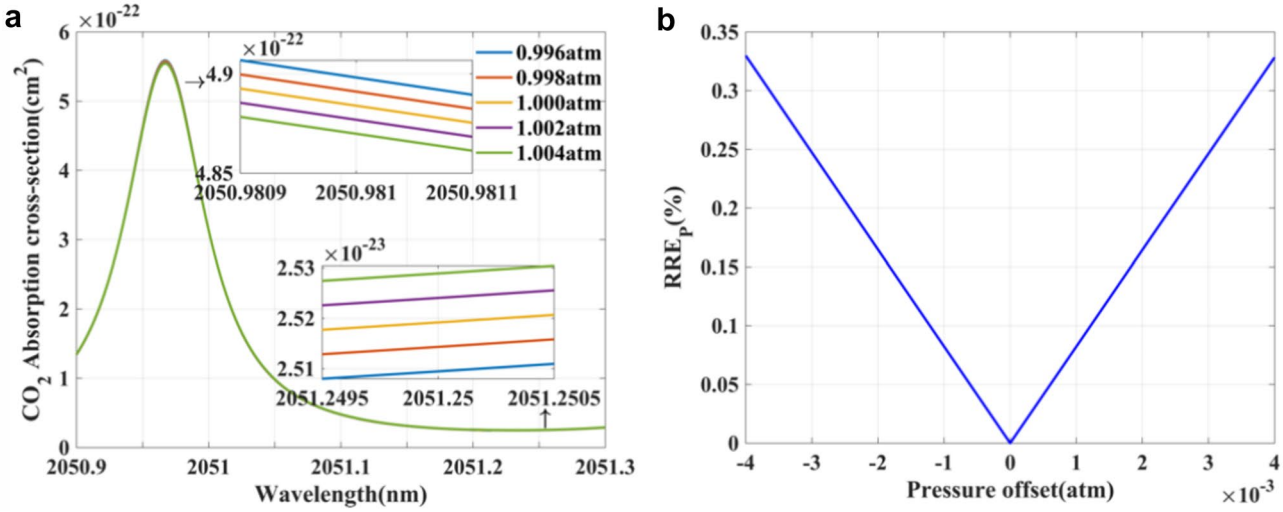

Figure. 7. (**a**) Local magnification at the absorption peak and absorption valley with different pressures; (**b**) Relationship between RRE_P and pressure offset.

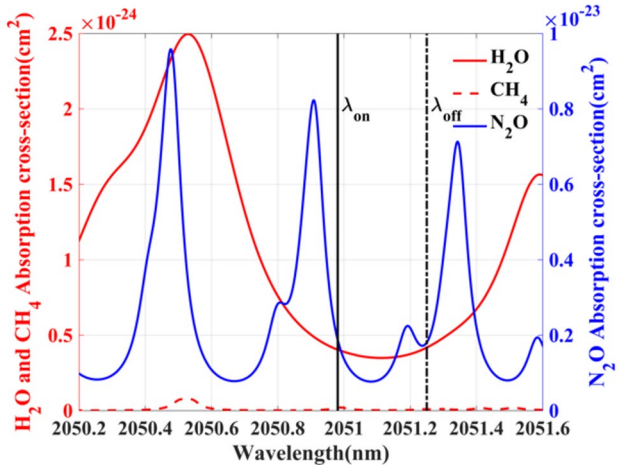

Figure 8. Absorption cross-section curves of H_2O, CH_4, and N_2O.

the CO_2 concentration under identical conditions. Therefore, in the same atmospheric environment, water vapor has an equivalent extinction effect to CO_2, and the corresponding RRE_G is approximately 0.19%. Hence, the lidar system can work normally in rainy weather and has good concentration resolution. Figure 8 also shows that the differential absorption cross-section of CH_4 is 1.04×10^{-26} cm^2, and the CH_4 concentration in the atmosphere is approximately 2 ppm, which is equivalent to the change in CO_2 absorption cross-section by 1.3832×10^{-27} cm^2, and the error caused by CH_4 is approximately 0.00001%, which can be ignored. The differential absorption cross-section of N_2O is 7.61×10^{-26} cm^2; if the N_2O concentration is 0.3 ppm in the atmosphere, the error caused by N_2O is approximately 0.00001%, which is also negligible.

Relative system error

Linewidth

Relative errors that may arise from the spectra of the radiation were investigated by substituting the absorption cross-section, which is only valid for monochromatic light, with the effective absorption cross-section. If $\tau_r/\tau_f = 1/3$ for the rise and fall time, a near monochromatic laser line ($\gamma \leq 10$ MHz) was assumed in simulation. Three typical laser Lorentz line shapes are drawn in Fig. 9a. As a result, the energy distribution is wider, and the effective energy is lower with the wider laser linewidth. Thus, a narrow linewidth laser has a higher output center energy. Assuming that the off-line absorption is negligible, Fig. 9b shows the error caused by sounding in the wing of the absorption line and center-line. When the linewidth gradually increases, the relative error also sharply increases, which will seriously affect the concentration inversion accuracy. The linewidth of the order of several dozens of MHz is slightly difficult to prepare in the 2-μm range for a single-frequency laser, so the requirements can be appropriately relaxed. If the linewidth is ≤ 350 MHz, RSE_L of ν_{on} is approximately ≤ 0.25%.

Frequency stability

Different frequency stabilities are selected to calculate the molecular absorption with the Voigt line shape and fitted to obtain the OD. Figure 10a shows that a larger slope near the center-line corresponds to a greater error caused by the laser frequency stability. In the on-line selection, it is important to consider both frequency stability error and absorption effect, which cannot be too small. If the frequency stabilization control circuit performance is sufficient, the wavelength drift range will decrease. When the frequency stability is less than 2.4 MHz, the $RSE_F \leq 0.08\%$. Although the frequency jitter for off-line is very large due to its location on a gentle slope, its error has a much smaller effect than the on-line case. The error caused by the on-line wavelength offset and linewidth is usually considered in combination. Figure 10b shows that the wavelength offset has a stronger effect on the relative error than the linewidth.

Spectral purity

The formula shows that the DAOD and spectral purity are important factors that affect the detection accuracy of the system. Figure 11 shows the calculation results. The difficulty of developing high spectral purity lasers can be lessened by the smaller DAOD. The 120-m range resolution is sufficiently excellent for a range-resolution system: the calculated DAOD is 0.08, and the $RSE_S \leq 0.25\%$ with $P_e > 99.78\%$.

Results

The current technology is in the leading position for concentration resolutions below 1 ppm. Through the above error analysis, the random and systematic errors of various influencing factors are summarized in Table 3. The systematic errors of the lidar system can be further corrected, and the impact of system defects on the measurement accuracy can be minimized by improving the laser design and optimizing the retrieval algorithm.

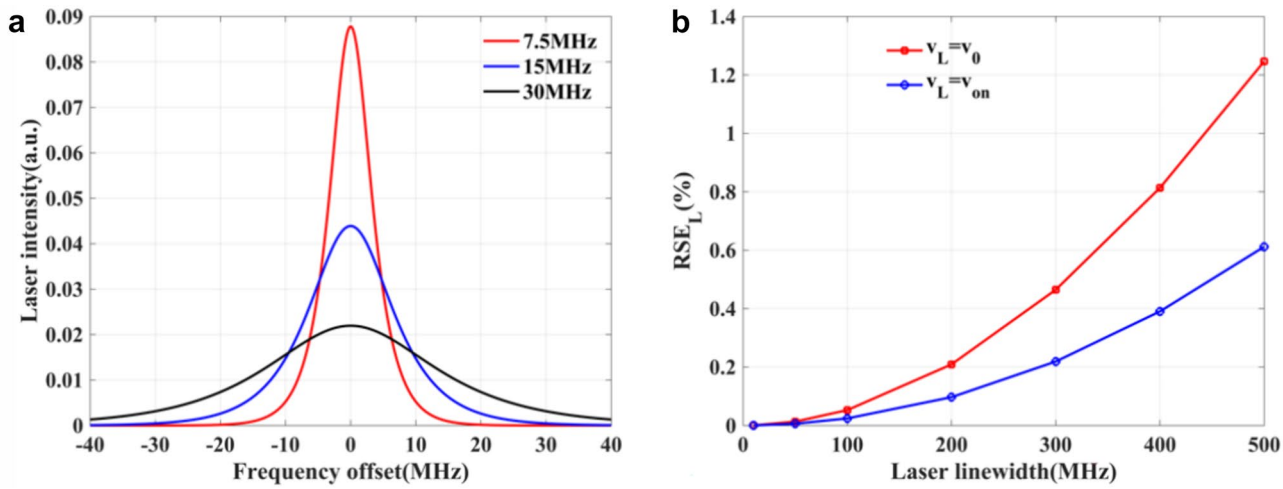

Figure 9. (**a**) Laser line shape. (**b**) RSE_L as a function of the laser linewidth for the center-line (squares) and soundings at the line wing (circles).

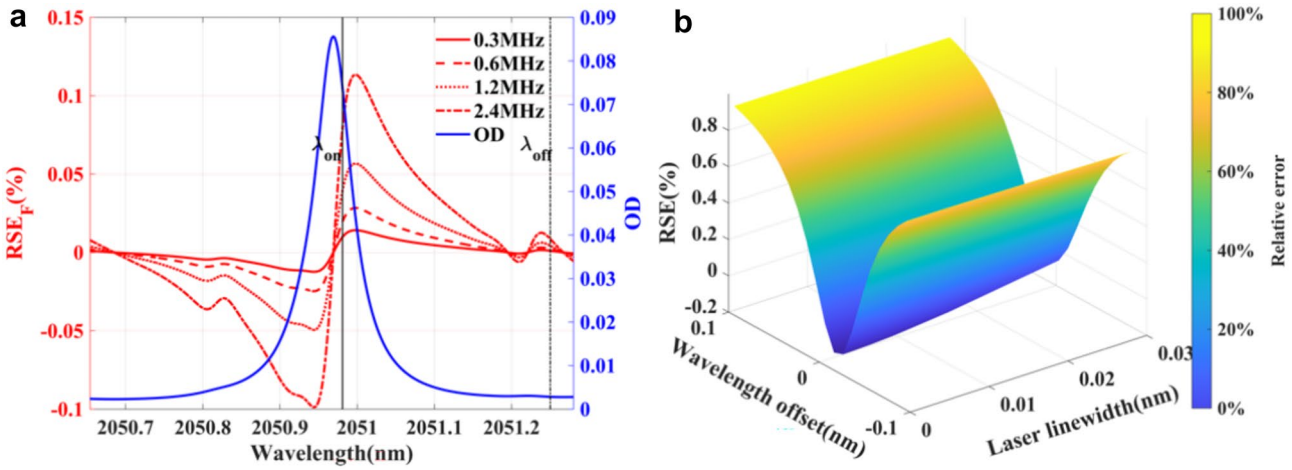

Figure 10. (**a**) RSE_F as a function of the laser frequency. (**b**) Error is caused by the wavelength offset and linewidth.

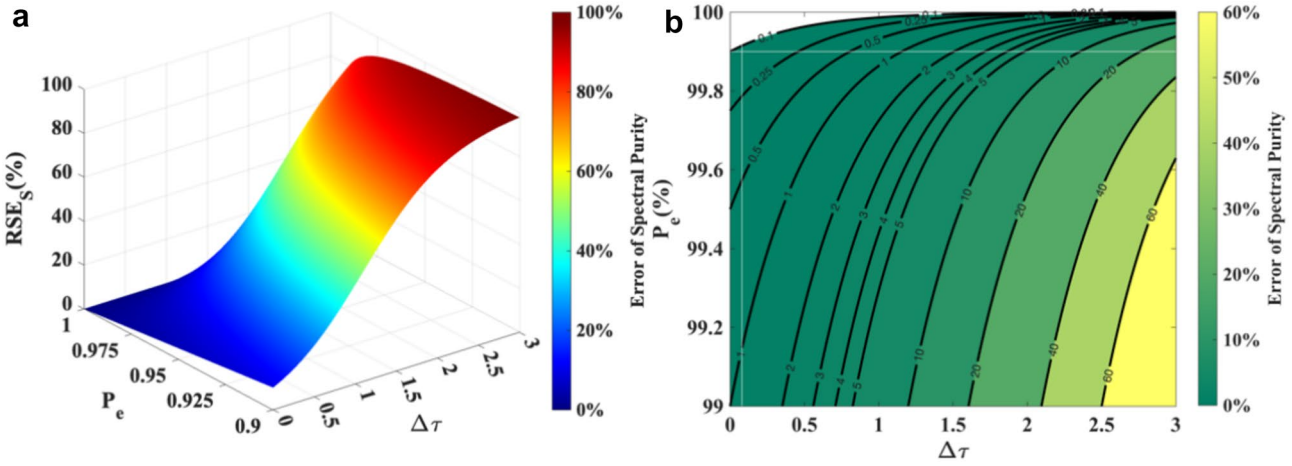

Figure 11. (**a**) RSE_S of the three-dimensional display caused by the spectral purity; (**b**) contour display of the spectral purity.

Error source	Uncertainty	Relative error
Temperature	− 0.7 to 0.7 K	0.25%
Pressure	− 0.003 to 0.003 atm	0.25%
Water vapor	≤ 100%	0.19%
Linewidth	≤ 350 MHz	0.25%
Frequency stability	≤ 2.4 MHz	0.08%
Spectral purity	≥ 99.78%	0.25%

Table 3. Errors of various error sources of RRDIAL.

The above analysis clearly shows that the laser frequency stability is the most critical factor that affects the measurement accuracy of the system and should receive focus during the lidar design. Next, the narrow-linewidth and high-spectral-purity lasers should be used as much as possible to enhance the system performance. The selection of a pressure-insensitive wavelength pair is preferred over the temperature factor. Finally, the influence of water vapor and other gases during the detection process is low, which indicates that the lidar system can detect CO_2 concentrations even in rainy weather.

Conclusion

In this study, the performance and system simulation of RRDIAL were evaluated by analyzing the detection uncertainty of the range and time-resolved concentration of CO_2. Firstly, The line-by-line radiation and transmission model based on the HITRAN 2020 database was constructed to calculate the absorption spectra of CO_2; then, the echo signal, SNR, and detection sensitivity were simulated by introducing several system analysis models with assumed parameters. The effects of the pulse energy, repetition frequency, and photodetector performance on the detection were discussed. A comparison with the existing detection system validated the simulation results. Finally, the optimal detection distance and concentration resolution of the simulated system were provided.

The US 1976 standard atmosphere model was used to simulate the relative random errors of several types of sources in various atmospheric circumstances. The calculation clearly shows that the temperature and pressure have less influence in a stable atmospheric environment, but introduced large errors when the meteorological environment is more complicated. Water vapour in this band is absorbed significantly more than other gases and is one of the main sources of error. A longer detection distance can be obtained by choosing to detect in clear weather, which will also assist the CO_2 concentration inversion.

The analysis shows that frequency stability should be an important item in the laser design index. In addition, narrowing the laser linewidth and improving the spectral purity help reduce the lidar system error and improve the system detection ability.

Data availability

The datasets used and analyzed during the current study are available from the corresponding author upon reasonable request.

Received: 21 March 2024; Accepted: 19 July 2024
Published online: 27 July 2024

References

1. Manuel, Q. *et al.* Differential absorption lidar for volcanic CO2 sensing tested in an unstable atmosphere. *Opt. Express* **23**(5), 6634–6644 (2015).
2. Sakaizawa, D. *et al.* Development of a 1.6 micron differential absorption lidar with a quasi-phase-matching optical parametric oscillator and photon-counting detector for the vertical CO2 profile. *Appl. Opt.* **48**(4), 748–757 (2009).
3. Robert, T. *et al.* Differential Laser absorption spectrometry for global profiling of tropospheric carbon dioxide: Selection of optimum sounding frequencies for high-precision measurements. *Appl. Opt.* **42**(33), 6569–6577 (2003).
4. Dobbs, M. *et al.* Active Sensing of CO2 Emissions over Nights, Days, and Seasons (ASCENDS). *Environ. Sci.* **1**, 85–88 (2007).
5. Caron, J. *et al.* A-SCOPE: Objectives and concepts for an ESA mission to measure CO2 from space with a lidar. In *15th Coherent Laser Radar Conference* (2009).
6. Amediek, A. *et al.* Development of an OPO system at 1.57 μm for integrated path DIAL measurement of atmospheric carbon dioxide. *Appl. Phys. B* **92**, 295–302 (2008).
7. Abshire, J. *et al.* Airborne measurements of CO2 column concentrations made with a pulsed IPDA lidar using a multiple-wavelength-locked laser and HgCdTe APD detector. *Atmos. Meas. Tech.* **11**(4), 2001–2025 (2018).
8. Lin, B. *et al.* Atmospheric CO2 column measurements in cloudy conditions using intensity-modulated continuous-wave lidar at 1.57 micron. *Opt. Express* **23**(11), 582–593 (2015).
9. Tamer, F. *et al.* Double-pulse 2-μm integrated path differential absorption lidar airborne validation for atmospheric carbon dioxide measurement. *Appl. Opt.* **55**(15), 4232–4246 (2016).
10. Taylor, T. *et al.* Evaluating the consistency between OCO-2 and OCO-3 XCO2 estimates derived from the NASA ACOS version 10 retrieval algorithm. *Atmos. Meas. Tech.* **16**(12), 3173–3209 (2023).
11. Kuze, A. *et al.* Update on GOSAT TANSO-FTS performance, operations, and data products after more than 6 years in space. *Atmos. Meas. Tech.* **9**(6), 2445–2461 (2016).
12. Yang, D. *et al.* Detection of anthropogenic CO2 emission signatures with TanSat CO2 and with copernicus sentinel-5 precursor (S5P) NO2 measurements: First results. *Adv. Atmos. Sci.* **40**, 1–5 (2023).
13. Campbell, J. *et al.* Field evaluation of column CO2 retrievals from intensity-modulated continuous-wave differential absorption lidar measurements during the ACT-America campaign. *Earth Space Sci.* https://doi.org/10.1029/2019EA000847 (2020).
14. Yu, A. *et al.* Three-dimensional detection of CO2 and wind using a 1.57 μm coherent differential absorption lidar. *Opt. Express* **32**(12), 21134 (2024).
15. Grady, J. *et al.* Coherent differential absorption lidar measurements of CO2. *Appl. Opt.* **43**(26), 5092–5099 (2004).
16. Gibert, F. *et al.* 2-μm Ho emitter-based coherent DIAL for CO2 profiling in the atmosphere. *Opt. Lett.* **40**(13), 3093–3096 (2015).
17. Cadiou, J. *et al.* Direct detection range resolved carbon dioxide differential absorption lidar measurements in the 2 μm range. *Commer. Sci. Sens. Imaging* **10215**, 66–72 (2017).
18. Uchiumi, M. *et al.* Development of DIAL for CO2 and CH4 in the atmosphere. *SPIE Asia-Pac. Remote Sens.* **4893**, 141–149 (2003).
19. Amediek, A. *et al.* CHARM-F-a new airborne integrated-path differential-absorption lidar for carbon dioxide and methane observations: Measurement performance and quantification of strong point source emissions. *Appl. Opt.* **56**(18), 5182–5197 (2017).
20. Browell, E. *et al.* Differential absorption lidar (DIAL) measurements from air and space. *Appl. Phys. B* **67**, 399–410 (1998).
21. Didier, B. *et al.* Complementary study of differential absorption lidar optimization in direct and heterodyne detections. *Appl. Opt.* **45**(20), 4898–4908 (2006).
22. Platt, U. *et al.* Direct measurements of atmospheric CH2O, HNO2, O3, NO2, and SO2 by differential optical absorption in the near UV. *J. Geophys. Res.* **85**(C12), 7453–7458 (1980).
23. Cooke, B. *et al.* CO2 dial transmitter/receiver noise characterization and related correlated noise issues. *Int. Soc. Opt. Photonics* **2702**, 2–15 (1996).
24. Qiu, Z. *et al.* Weak signal detection system and noise analysis for aerosol detection lidar. *Proc. SPIE.* **7382**, 1284–1291 (2009).
25. Gordon, I. *et al.* The HITRAN2020 molecular spectroscopic database. *J. Quant. Spectrosc. Radiat. Transf.* **277**, 107949 (2022).
26. Caron, J. *et al.* Operating wavelengths optimization for a spaceborne lidar measuring atmospheric CO2. *Appl. Opt.* **48**(28), 5413–5422 (2009).
27. Ismail, S. *et al.* Airborne and spaceborne lidar measurements of water vapor profiles: A sensitivity analysis. *Appl. Opt.* **28**(17), 3603–3615 (1989).

28. Shibata, Y. *et al.* Development of 1.6 μm DIAL using an OPG/OPA transmitter for measuring atmospheric CO2 concentration profiles. *Appl. Opt.* **56**(4), 1194–1201 (2017).
29. Ehret, G. *et al.* Space-borne remote sensing of CO2, CH4, and N2O by integrated path differential absorption lidar: A sensitivity analysis. *Appl. Phys. B* **90**, 593–608 (2008).
30. Caron, J. *et al.* Performance modeling for A-SCOPE: A space-borne lidar measuring atmospheric CO2. *Remote Sens.* https://doi.org/10.1117/12.830364 (2009).
31. Sakaizawa, D. *et al.* Ground-based demonstration of a CO2 remote sensor using a 1.57 μm differential laser absorption spectrometer with direct detection. *J. Appl. Remote Sens.* **4**, 043548 (2010).
32. Ambrico, P. *et al.* Sensitivity analysis of differential absorption lidar measurements in the mid-infrared region. *Appl. Opt.* **39**(36), 6847–6865 (2000).
33. Kochanov, R. *et al.* HITRAN application programming interface (HAPI): A comprehensive approach to working with spectroscopic data. *J. Quant. Spectrosc. Radiat. Transf.* **117**, 15–30 (2016).
34. Hashemi, R. *et al.* Revising the line-shape parameters for air- and self-broadened CO2 lines toward a sub-percent accuracy level. *J. Quant. Spectrosc. Radiat. Transf.* **256**, 107283 (2020).
35. Koch, G. *et al.* Side-line tunable laser transmitter for differential absorption lidar measurements of CO2: Design and application to atmospheric measurements. *Appl. Opt.* **47**(7), 944–956 (2008).
36. Cadiou, E. *et al.* Atmospheric boundary layer CO2 remote sensing with a direct detection LIDAR instrument based on a widely tunable optical parametric source. *Opt. Lett.* **42**(20), 4044–4047 (2017).
37. Weitkamp, C. *Lidar, Range-Resolved Optical Remote Sensing of the Atmosphere* (CRC Press, 2005).
38. Bradly, J. *et al.* Analysis and design methodology for the development of optimized direct detection CO2 DIAL receivers. *Opt. Photonics* **3122**, 1–36 (1997).
39. Refaat, T. *et al.* Backscatter 2-mu m lidar validation for atmospheric CO2 differential absorption lidar applications. *IEEE Trans. Geosci. Remote Sens.* **49**(1), 572–580 (2011).

Acknowledgements

This study was supported by the National Key Research and Development Program of China (2022YFC3700400) and the National Natural Science Foundation of China (42005106).

Author contributions

Zhang, B. W. wrote the manuscript and calculated the data. Fan, G. Q., and Zhang, T. S. provided guidance on professional knowledge. All authors reviewed the manuscript.

Competing interests

The authors declare no competing interests.

Additional information

Correspondence and requests for materials should be addressed to G.F. or T.Z.

Reprints and permissions information is available at www.nature.com/reprints.

Publisher's note Springer Nature remains neutral with regard to jurisdictional claims in published maps and institutional affiliations.